

See Silhouettes in Motion with Neuromorphic Vision

Pei Zhang, *Member, IEEE*, Shijie Lin, *Graduate Student Member, IEEE*, Zhou Ge, *Member, IEEE*, Jinpeng Chen, *Member, IEEE*, and Wei Pu, *Member, IEEE*

Abstract—Quasi-bimodal objects, such as text, road signs, and barcodes, play a basic yet vital role in daily visual communication. By boiling these down to clear silhouettes, binarization uses a minimal language to convey essential vision cues for maximum downstream efficiency. The catch is that frame-based imaging often struggles on mobile platforms like drones, self-driving cars, and underwater vehicles. In these dynamic scenes, rapid motion and harsh lighting can make it blind, causing severe motion blur and erasing crucial details. To overcome the limits, neuromorphic vision via event cameras, featuring microsecond-level temporal resolution and high dynamic range, steps in as a natural solution. Building upon this event-driven sensing paradigm, we introduce a simple yet effective dual-modal approach that harnesses the synergy between frames and events to achieve real-time, high-frame-rate binarization on CPU-only devices. Extensive evaluations present that it earns competitive performance against leading techniques in reducing motion blur, while delivering impressive improvements under challenging illumination. Besides, our asynchronous workflow bypasses event scarcity that breaks traditional time-binning reconstruction, maintaining clear target shapes even at extreme kilohertz frame rates. Its binary results further serve as reliable representations that facilitate a range of downstream tasks. This work paves the way towards lightweight perception and interaction in embodied intelligence on resource-constrained edge platforms.

Index Terms—Event camera, neuromorphic vision, image binarization, real time, high frame rate, dual modality.

I. INTRODUCTION

CONSIDER a common night-driving scenario in Fig. 1: glaring high beams from a trailing vehicle strike a reflective traffic sign ahead. Just as sudden glare blinds a human driver, onboard image sensors with limited dynamic range fail similarly. Due to inherent latency, the auto-exposure system struggles to quickly reduce light intake. Together with a slow shutter required for nighttime low light, this delay causes partial saturation that washes out the sign while leaving motion blur and ghosting. In such urgent cases, either conventional edge detection techniques or modern multimodal large language models (MLLMs) fail to offer reliable feedback since

Pei Zhang is with the School of Electrical Engineering, Guangxi University (e-mail: pzhang@gxu.edu.cn).

Shijie Lin is with the Department of Computer Science, The University of Hong Kong (e-mail: lsj2048@connect.hku.hk).

Zhou Ge is with the School of Mechatronic Engineering and Automation, Shanghai University, and also with the SHU General Intelligent Robotics Research Institute (e-mail: gezhou@shu.edu.cn).

Jinpeng Chen is with the School of Computer Science (National Pilot Software Engineering School), Beijing University of Posts and Telecommunications (e-mail: jpchen@bupt.edu.cn).

Wei Pu is with the School of Information and Communication Engineering, University of Electronic Science and Technology of China (e-mail: puwei@uestc.edu.cn).

Corresponding author: Pei Zhang. This work was partially completed during his study at The University of Hong Kong.

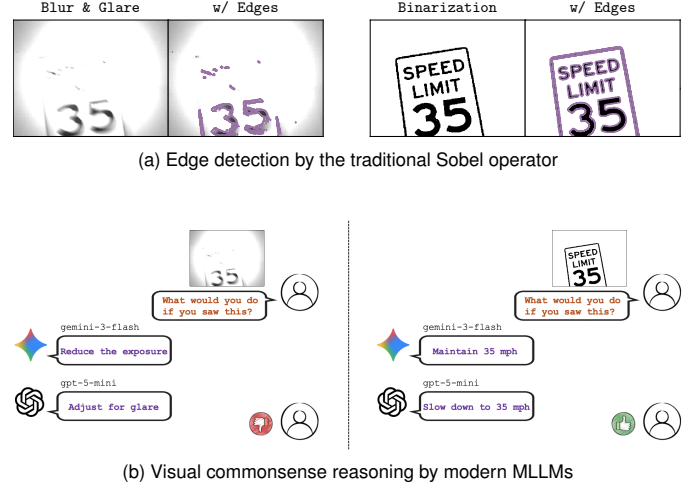


Fig. 1. Minimal input, maximum insight.

they are bottlenecked by the loss of raw visual information. Bridging this perception gap is our motivation.

Quasi-bimodal objects can be found everywhere in our daily lives, like text, road signs, and barcodes. Checkerboards, fiducials are often used for camera calibration, localization, and tracking for robotics, AR/VR, and autonomous systems [1]–[3]. Binarization from images or frames, which can be taken as data compression pre-processing, uses a minimal language (*i.e.*, either 0 or 1) to describe the essential structure of a scene for maximum downstream efficiency across accuracy, runtime, and resource footprints. However, it is challenging to obtain clear bimodal silhouettes on mobile devices like drones, self-driving cars, and underwater vehicles, where image sensors are often blind by complex dynamics and harsh illumination.

To overcome the physical limits of frame-based imaging, event cameras offer a popular solution for real-time perception on mobile platforms, owing to their microsecond-level temporal resolution, high dynamic range (HDR, over 120 dB), and minimal resource footprints [4], [5]. The sparse, binary-like nature of event streams aligns well with binarization. However, their asynchronous shape is incompatible with downstream algorithms, as modern hardware accelerators favor synchronous, grid-based representations [6], [7]. Moreover, events encode intensity changes rather than absolute brightness, which is insufficient for recognizing certain objects (*e.g.*, QR codes) that demands dense spatial context beyond mere edges. Frame reconstruction thus remains necessary. While one could harness a step-wise pipeline that first goes through existing dual-modal motion deblurring [8]–[10] to obtain a sharp intensity frame and then uses established binarization methods [11], [12], this is suboptimal. The former is often computationally

intensive due to its reliance on deep learning or complex optimization. Besides, reconstruction artifacts can impair subsequent binarization, failing to satisfy the strict requirements for accuracy and computational efficiency. In practice, resource-constrained edge systems reserve their compute for demanding downstream models like MLLMs and squeeze allowable overhead for data pre-processing. Meanwhile, the pre-processing should keep pace with the rapid response of event cameras to avoid bottlenecks. This alignment preserves the hardware advantages and ensures end-to-end fast system responsiveness.

Building upon these observations, we propose a simple yet effective, lightweight, and dual-modal method that leverages the synergy between frames and events for unified, single-step binarization. By self-adaptive modulation, it delivers faithful binarization under severe motion blur and harsh illumination. With linear time complexity, it comfortably achieves real-time performance on CPU-only platforms. Also, its asynchronous nature bypasses event scarcity that breaks traditional time-binning reconstruction and decouples computational overhead from frame rates, preserving clear target shapes with constant low latency at extreme kilohertz scales. Its binary results also provide reliable representations that benefit downstream tasks like text recognition, object tracking, and optical flow estimation. Such a solution holds strong potential to bridge the gap between high-speed sensing and efficient edge computation.

The remainder of this paper is organized as follows. Section II briefly reviews related work. Section III presents the proposed dual-modal binarization method. Section IV details the experimental design and reports comparative evaluations against existing techniques. Section V concludes the work with a discussion of key findings and limitations.

II. RELATED WORK

A. Image Binarization

Image binarization, which can be taken as data compression, is a fundamental pre-processing for high-level vision tasks. Early approaches hinge on global statistical analysis [11], [13] or local adaptive thresholding [14], [15] to separate foreground from background. While computationally efficient, they often struggle with texture degradation under harsh illumination and leave unstable performance. The advance of deep learning shifts the focus towards semantic segmentation, where convolutional neural networks (CNNs) learn hierarchical representations across either pixels or patches [16], [17]. Despite their improved robustness, these frame-based methods remain constrained by the limited temporal resolution of traditional image sensors. Thus, motion blur is treated as spatial artifacts to be painfully reconstructed rather than temporal signals to be naturally captured, often bringing structural distortions, loss of fine details, and temporal inconsistency among frames [18]. Such challenges make frame-based solutions impractical for real-world dynamic scenes beyond controlled lab conditions [19].

B. Event Cameras

Event cameras pose a paradigm shift in visual perception. As opposed to frame-based imaging that captures absolute intensity at a fixed frame rate, they asynchronously measure

per-pixel changes in brightness and generate continuous event streams in response to scene dynamics [4]. Naturally, the resulting sparse, spike-like streams are incompatible with mainstream vision frameworks that favor synchronous representations, which has been driving the search for alternative modeling techniques [20]. Such a biologically inspired mechanism offers several attractive features, including microsecond-level temporal resolution, HDR, ultra-low latency, and minimal resource consumption. Accordingly, they have received growing attention across a wide range of domains, including agile aerial robotics [21], [22], high-speed advanced manufacturing [23]–[25], quantum sensing [26], and biological research [27]–[29]. With the rapid rise of embodied intelligence driving the need for real-time, energy-efficient visual systems, event cameras provide an alternative for robust performance under challenging imaging conditions [30], [31].

C. Dual-Modal Motion Deblurring

Event cameras offer a viable solution to bypass the temporal limitations of frame-based sensors, enabling blur-free capture of high-speed motion under challenging illumination. To bridge the precise measurement with visual reconstruction, various computational paradigms have been developed. Model-based approaches, which establish physical mappings between event streams and latent sharp frames, typically offer fast responsiveness, CPU-only feasibility, and rigorous interpretability [10], [32], [33]. Concurrently, the rapid advancement of learning-based techniques fosters the exploration of dual-modal frame-event synergy for motion deblurring, spanning from discriminative backbones (*e.g.*, CNNs [34]–[36], Transformers [37], Mamba [38]) to emerging generative strategies (*e.g.*, diffusion [39], [40]). While these methods earn state-of-the-art reconstruction fidelity, they often come at the cost of prohibitive computational complexity and introduce substantial redundancy for binary representations. Consequently, they are ill-suited for efficient binarization and fail to meet the strict speed and resource requirements for real-time applications.

D. Dual-Modal Binarization

Directly shaping binary motion signals from frame-event synergy is a shift that bypasses the high computational overhead of full-scale intensity reconstruction. Despite its potential, research in this branch remains nascent. One pioneering effort frames this task as a pixel-wise binary classification problem and achieves high-frame-rate performance on CPU-only systems [41]. Nevertheless, it underuses the HDR features of events and then suffers from performance degradation under non-ideal or volatile illumination. Such sensitivity to lighting conditions restricts its deployment in unpredictable real-world environments. Beyond algorithmic efficiency, the industrial significance of this task is recently highlighted by the integration of event cameras into smart glasses for low-power optical character recognition (OCR) [42]. Thus, developing a fast, lightweight, dual-modal binarization framework resilient across diverse lighting is not merely an incremental improvement, but a prerequisite for reliable real-time vision on resource-constrained edge platforms.

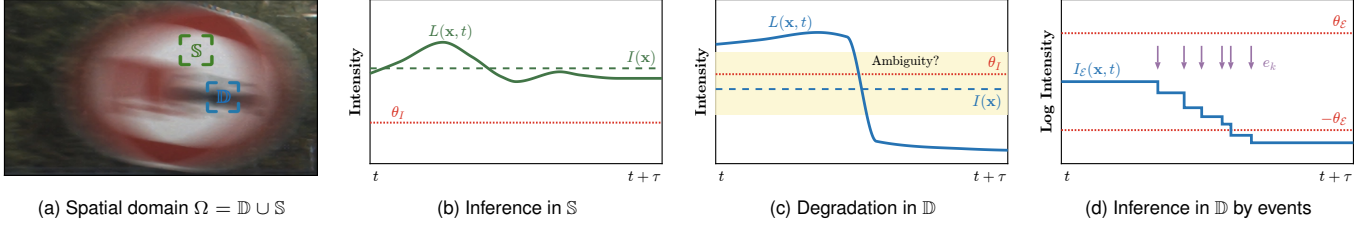


Fig. 2. The dual-modal binarization framework. (a) A blurry “No overtaking” sign observed during high-speed driving is spatially decomposed into \mathbb{D} and \mathbb{S} . (b) Static pixels are faithfully binarized using $I(\mathbf{x})$ and θ_I . (c) Motion blur in \mathbb{D} pushes $I(\mathbf{x})$ into an ambiguity zone, causing intensity-based inference to fail. (d) Dynamic pixels are resolved by integrating events, where we decode the sharp binary state via $\pm\theta_{\mathcal{E}}$.

III. METHODOLOGY

A. Dual-Modal Binarization Framework

1) *Problem Definition*: Our objective is to recover a temporally dense, sharp binary video sequence from motion-blurred intensity frames and their corresponding asynchronous events. We define the latent sharp scene radiance as $L(\mathbf{x}, t)$, where \mathbf{x}, t denote spatial pixel coordinates and time, respectively. The active-pixel sensor (APS) accumulates photons over an exposure interval $\mathcal{T} = [t, t + \tau]$ with duration τ . In dynamic scenes, the captured intensity frame $I(\mathbf{x})$ represents a temporal integration of the time-varying scene radiance, often exhibiting severe motion blur

$$I(\mathbf{x}) = \frac{1}{\tau} \int_{\mathcal{T}} L(\mathbf{x}, t) dt. \quad (1)$$

For bimodal scenes, $L(\mathbf{x}, t)$ ideally comprises two intensity levels, foreground and background. However, temporal integration blends them along motion trajectories to destroy high-frequency spatial cues essential for accurate binarization.

In parallel, the dynamic vision sensor (DVS)¹ generates a stream of events $\mathcal{E} = \{e_k\}_{k=1}^K$, where K is the cardinality of \mathcal{E} . Each event $e_k = (\mathbf{x}_k, t_k, p_k)$, indexed by k , is triggered asynchronously when the logarithmic intensity at pixel \mathbf{x}_k changes by a temporal contrast threshold c

$$\ln L(\mathbf{x}_k, t_k) - \ln L(\mathbf{x}_k, t_k - \Delta t_k) = p_k c, \quad (2)$$

where Δt_k is the time elapsed since the last event at \mathbf{x}_k , and $p_k \in \{+1, -1\}$ denotes the polarity. In this context, dual-modal binarization seeks a mapping f that reconstructs a sharp binary frame $B(\mathbf{x}, t) \in \{0, 1\}$ for any time $t \in \mathcal{T}$ using both the blurry observation and the event stream

$$B(\mathbf{x}, t) = f(I(\mathbf{x}), \mathcal{E}; t). \quad (3)$$

Motion blur corrupts the intensity integration at transitional boundaries, whereas static regions remain consistent. Taking binarization as activity-based pixel-wise classification [41], we decompose the spatial domain $\Omega = \mathbb{D} \cup \mathbb{S}$ into two disjoint subsets, dynamic \mathbb{D} and static \mathbb{S} , as in Fig. 2. Pixels $\mathbf{x} \in \mathbb{D}$ correspond to locations experiencing significant radiance transitions during \mathcal{T} , where $I(\mathbf{x})$ becomes a linear combination of foreground and background values. Conversely, for $\mathbf{x} \in \mathbb{S}$, the integration in Eq. (1) degenerates to a scaling of the constant latent state, making $I(\mathbf{x})$ a valid proxy for binarization. Then,

¹For example, the DAVIS346 event camera integrates a DVS and an APS within the same pixel array, with each pixel sharing a single photodiode [43].

we reformulate f as the union of two independent inference operators, $f_{\mathcal{E}}$ (event-driven) and f_I (intensity-based), targeting a specific reference time $t' \in \mathcal{T}$

$$B(\mathbf{x}, t') = \mathbb{I}_{\mathbf{x} \in \mathbb{D}} f_{\mathcal{E}}(\mathcal{E}; \mathbf{x}, t') + \mathbb{I}_{\mathbf{x} \in \mathbb{S}} f_I(I(\mathbf{x})). \quad (4)$$

Here, $f_{\mathcal{E}}$ leverages the microsecond-level temporal resolution of events to decode the binary state from moving edges aligned to t' , while f_I resolves static regions using global intensity statistics. This formulation isolates the ill-posed motion deblurring problem to the sparse \mathbb{D} naturally captured by event cameras, thereby maximizing computational efficiency.

2) *Inference in Event Space*: We recover $B(\mathbf{x}, t')$, $\mathbf{x} \in \mathbb{D}$ by integrating events to detect significant polarity shifts. Let $I_{\mathcal{E}}(\mathbf{x}, t')$ be the accumulated logarithmic intensity change up to t'

$$I_{\mathcal{E}}(\mathbf{x}, t') = c \sum_{e_k \in \mathcal{E}} p_k \delta(\mathbf{x} - \mathbf{x}_k) \mathcal{H}(t' - t_k), \quad (5)$$

where δ is the Kronecker delta, and \mathcal{H} denotes the Heaviside step function. By causality, a brightness rise implies the pixel started from dark (0), and a drop implies it started from bright (1). We then define $f_{\mathcal{E}}$ by an event-driven confidence threshold $\theta_{\mathcal{E}}$

$$f_{\mathcal{E}}(\mathcal{E}; \mathbf{x}, t') = \begin{cases} 0 & \text{if } I_{\mathcal{E}}(\mathbf{x}, t') \geq \theta_{\mathcal{E}}, \\ 1 & \text{if } I_{\mathcal{E}}(\mathbf{x}, t') \leq -\theta_{\mathcal{E}}. \end{cases} \quad (6)$$

Pixels that do not accumulate sufficient contrast (*i.e.*, $|I_{\mathcal{E}}| < \theta_{\mathcal{E}}$) despite being in \mathbb{D} are treated as ambiguous and reassigned to the intensity-based inference branch.

3) *Inference in Intensity Space*: For $\mathbf{x} \in \mathbb{S}$, $I(\mathbf{x})$ remains a proxy for the latent state. We apply an intensity binarization threshold θ_I

$$f_I(I(\mathbf{x})) = \begin{cases} 1 & \text{if } I(\mathbf{x}) > \theta_I, \\ 0 & \text{otherwise.} \end{cases} \quad (7)$$

Such a dual-modal binarization framework leaves the key parameters $c, \theta_{\mathcal{E}}, \theta_I$ up in the air, which are elaborated upon subsequent sections.

B. Adaptive Parameter Estimation

1) *Online Temporal Contrast Estimation*: Assuming c to be a time-invariant constant fails in real-world scenes where DVS sensitivity drifts frequently, which often leads to reconstruction bias [33]. Observing that global shifts dominate stochastic inter-pixel mismatches, we bypass costly per-pixel calibration in favor of adaptive sensitivity tracking. This rapidly

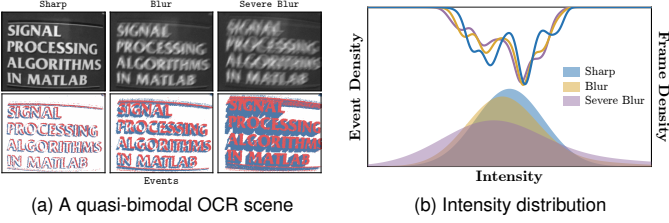


Fig. 3. Stronger motion brings heavier frame blur, yet the distribution in a quasi-bimodal scene remains preserved and informative (curves). Meanwhile, events increase and become more spatially dispersed along the motion trajectory (shades). In both cases, structural responses are spread rather than concentrated, resulting in reduced photometric variance.

stabilizes event computation against temporal instability from lighting fluctuations. Thus, we propose an online log-domain variance matching estimator. Our key insight builds on the statistical stability of quasi-bimodal scenes, where the photometric spread is dominated by inter-class separation between foreground and background rather than intra-class texture variations. While motion blur degrades high-frequency edges, the global statistical dispersion, anchored by the dominant intensity peaks, remains sufficiently informative for contrast estimation as long as histogram separability is not fully destroyed. As shown in Fig. 3, motion blur does not reshape the distribution yet reduces the variance in both frames and events [44], [45]. Derived from Eqs. (2) and (5), we thus align the two modalities by matching their variances σ^2 over $\mathbf{x} \in \mathbb{D}$

$$\sigma_{\mathbb{D}}^2 \left(\ln (G_{\tilde{\sigma}} * I(\mathbf{x}) + \epsilon) \right) \approx c^2 \cdot \sigma_{\mathbb{D}}^2 (E(\mathbf{x}, t')), \quad (8)$$

where $G_{\tilde{\sigma}}$ denotes a Gaussian kernel with a scale $\tilde{\sigma}$ to suppress sensor artifacts, ϵ is a small offset, and $E(\mathbf{x}, t') \triangleq \sum p_k \delta(\mathbf{x} - \mathbf{x}_k) \mathcal{H}(t' - t_k)$ represents an accumulated event frame. We also restrict the operation to \mathbb{D} to improve computational efficiency and avoid instability in static regions. Solving Eq. (8) yields an instantaneous estimate \hat{c} , yet relying solely on per-frame estimation is prone to induce temporal flickering. We then update c by an exponential moving average across frames

$$c_n = \alpha \cdot \hat{c}_n + (1 - \alpha) \cdot c_{n-1}, \quad (9)$$

where n is the index of intensity frames, and $\alpha \in [0, 1]$ controls the adaptation rate. This temporal smoothing prevents abrupt scale divergence and preserves inter-frame consistency even when instantaneous estimates are degraded under extreme illumination. Different from iterative optimization [10], this $\mathcal{O}(K)$ closed-form solution offers real-time adaptability to illumination changes without the need of offline calibration or pre-training [46].

2) *Dynamic Range Reshaping*: High-quality binarization hinges on histogram separability. However, $I(\mathbf{x})$ may undergo saturation or photon noise for overexposure or underexposure, causing the histogram to collapse into a flat or unimodal distribution in which structural information is buried. To recover a separable distribution, we propose a dynamic range reshaping strategy via exposure-adaptive fusion. We first quantify an exposure quality $\lambda = \exp(-\beta(\mu_I - \mu)^2) \in (0, 1]$ based on the deviation of the mean μ_I of $I(\mathbf{x})$ from an ideal mid-gray

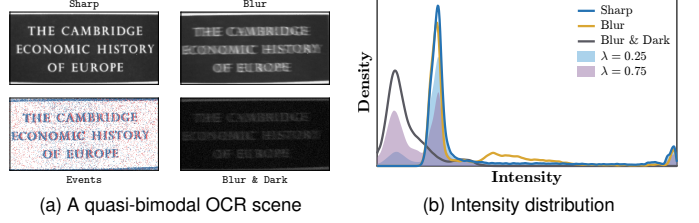


Fig. 4. A clear bimodal shape is observed in the sharp scene, while motion blur & dark reduces class separability. We leverage the event prior ($\lambda = 0.25$) to recover the missing structural details as well as a separable distribution.

$\mu = 0.5$, where β controls sensitivity. A $\lambda \rightarrow 1$ indicates well-balanced exposure, while $\lambda \rightarrow 0$ signals distribution collapse. We then fuse a proxy frame $I_{\lambda}(\mathbf{x})$ to correct histogram statistics, formulated as a convex combination of the observed intensity and an event-driven prior

$$I_{\lambda}(\mathbf{x}, t') = \lambda I(\mathbf{x}) + (1 - \lambda) (\mathbb{I}_{\mathbf{x} \in \mathbb{D}} \cdot \tilde{I}_{\mathcal{E}}(\mathbf{x}, t') + \mathbb{I}_{\mathbf{x} \in \mathbb{S}} \cdot \mu), \quad (10)$$

where $\tilde{I}_{\mathcal{E}}(\mathbf{x}, t') = \exp(I_{\mathcal{E}}(\mathbf{x}, t'))$ is the event integral. This formulation reshapes histogram separability via a dual mechanism tailored to the signal nature, which comprises dynamic restoration and static regularization. In dynamic regions where motion blur and exposure imbalance co-occur, we leverage the HDR property of events to recover degraded structural features. As $\lambda \rightarrow 0$, the fusion prioritizes the prior from events to restore histogram peaks. Meanwhile, in static regions where poor exposure manifests as high-frequency photon noise or clamping, we apply variance compression by pulling pixels towards a neutral pivot. As a result, $I_{\lambda}(\mathbf{x})$ enhances histogram separability by reinforcing inter-class contrast and suppressing intra-class dispersion, which facilitates the identification of an optimal separating hyperplane even when intensity frames are severely degraded. Fig. 4 illustrates an OCR scene [33] and its corresponding distribution to explain the process.

Discussion on Observability & Extreme Cases. Eq. (8) assumes that $I(\mathbf{x})$ retains sufficient spatial observability. Under moderate exposure imbalance, both log-domain compression and temporal smoothing retain reliable contrast scaling, but severe saturation is prone to bias the variance estimate. The issue becomes ill-posed only when both intensity frames and events lose perceptual information (e.g., bright glare with slight motion, as some letters in Fig. 5), leaving no recoverable contrast cues in either modality. Notably, Eqs. (8) and (10) operate at distinct layers more than a dependency. Estimating c calibrates the global event amplitude to the intensity scale across varying illumination, which maximizes histogram separability for precise binarization. Even if c degrades under extreme exposure, the bias primarily affects the contrast magnitude rather than topological integrity. Since the binarization task targets inter-class separability instead of exact radiance, moderate scale deviations do not induce misclassification. Failure occurs only at the observability limit, where neither modality conveys sufficient discriminative features.

3) *Optimal Threshold Estimation*: Once reshaped, $I_{\lambda}(\mathbf{x}, t')$ yields an optimized bimodal distribution for thresholding. While traditional Otsu maximizes a statistical inter-class variance $\sigma_b^2(\theta)$ to identify thresholds [13], it is inherently spatially

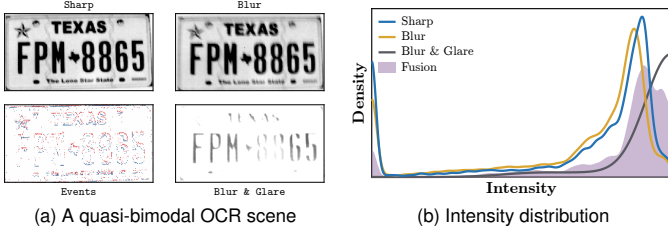


Fig. 5. A clear bimodal shape is observed in the sharp scene, while motion blur & glare shows unimodal distribution. Despite their HDR, event cameras respond to slight motion with limited events that fail to complement the saturated frame with sufficient features, leading to ineffective fusion and a suboptimal distribution.

blind and overlooks any high-frequency spatial cues restored in $I_\lambda(\mathbf{x}, t')$. When histogram peaks are shifted by residual noise or saturation artifacts, a pure statistical threshold may drift away from physical boundaries, leading to suboptimal results. To bridge this gap, we propose a gradient-aware Otsu estimator incorporating spatial priors through a gradient density term

$$g(\theta) = \sum_{\mathbf{x}: I_\lambda(\mathbf{x}, t') = \theta} \|\nabla I_\lambda(\mathbf{x}, t')\|, \quad (11)$$

defined as the cumulative gradient magnitude of all pixels at a candidate intensity level θ . This acts as an anchor to pull θ towards the sharpest edges in $I_\lambda(\mathbf{x}, t')$. We then formulate a hybrid objective that favors the estimate θ^* by jointly maximizing statistical separability and structural consistency

$$\theta^* = \arg \max_{\theta} \sigma_b^2(\theta) \cdot \ln(1 + g(\theta)), \quad (12)$$

where $\ln(1 + g(\theta))$ penalizes thresholds in low-gradient, flat regions and rewards those aligned with the restored edges in \mathbb{D} . While θ^* provides a global baseline, the quantization of intensity levels may introduce slight deviations. To ensure precise boundary alignment, θ_I is refined by seeking the local gradient ridge within a narrow 2% neighborhood $\mathcal{N}(\theta^*)$

$$\theta_I = \arg \max_{\theta \in \mathcal{N}(\theta^*)} g(\theta). \quad (13)$$

This snaps θ_I to the exact peak of the physical contrast step, resolving ambiguity between statistically optimal and spatially faithful boundaries. To maintain dual-modal consistency, $\theta_\mathcal{E}$ is obtained by mapping θ_I to event space

$$\theta_\mathcal{E} = \theta_I \cdot \max_{\mathbf{x} \in \mathbb{D}} |I_\mathcal{E}(\mathbf{x}, t')|, \quad (14)$$

which ensures $f_\mathcal{E}$ and f_I operate on a unified decision space. By such a statistical-structural coupling, the estimator resolves ambiguity in the separating hyperplane that ensures consistent binarization performance across varying imaging conditions.

C. High-Frame-Rate Video Generation

With c , θ_I , $\theta_\mathcal{E}$ determined, we obtain a static binary snapshot $B(\mathbf{x}, t)$ at any time. However, recovering the continuous temporal evolution of a scene via frame-by-frame reconstruction is computationally redundant and prone to temporal jitter. As such, we propose an asynchronous state propagation strategy that treats the initial binary frame as a seed and propagates it

Algorithm 1: Asynchronous State Propagation

Input: $B(\mathbf{x}, t_0)$, \mathcal{E} , c and $\theta_\mathcal{E}$

Output: $B(\mathbf{x}, t)$

```

1 Initialize  $r(\mathbf{x}) \leftarrow 0$  for all  $\mathbf{x}$ 
2 foreach  $e_k = (\mathbf{x}_k, t_k, p_k) \in \mathcal{E}$  do
3   if  $B(\mathbf{x}_k) \oplus \frac{1+p_k}{2}$  then
4      $r(\mathbf{x}_k) \leftarrow r(\mathbf{x}_k) + p_k \cdot c$ 
5     if  $|r(\mathbf{x}_k)| \geq \theta_\mathcal{E}$  then
6        $B(\mathbf{x}_k) \leftarrow 1 - B(\mathbf{x}_k)$ 
7        $r(\mathbf{x}_k) \leftarrow 0$ 
8        $B(\mathbf{x}_k) \leftarrow \mathbb{I}[\sum_{\mathbf{x}' \in \mathcal{W}} B(\mathbf{x}') > \frac{1}{2}|\mathcal{W}|]$ 

```

asynchronously to the temporal domain, driven solely by inter-frame events. This reformulates the video generation problem from dense reconstruction into a sparse, event-driven update process, thus minimizing latency and computational load.

As shown in Algorithm 1, we model the binary transition of each pixel as a state-dependent accumulation process. Instead of complex global optimization, we only track a residual $r(\mathbf{x}, t)$ that records incremental changes relative to the current state. For each incoming event, we update the residual at a specific \mathbf{x} based on its prior state

$$r(\mathbf{x}, t_k) = r(\mathbf{x}, t_{k-1}) + p_k \cdot c \cdot \mathbb{I}\left[B(\mathbf{x}, t_{k-1}) \oplus \frac{1+p_k}{2}\right], \quad (15)$$

where the indicator function activates only when p_k opposes the current state. If a pixel is already bright, we explicitly ignore positive events and only accumulate negative ones. Such a mechanism also functions as noise filtering where small radiance fluctuations or redundant events that are insufficient to trigger a flip are effectively suppressed. Then, $B(\mathbf{x}, t_k)$ remains unchanged until the residual sufficiently accumulates

$$B(\mathbf{x}, t_k) = \begin{cases} 1 - B(\mathbf{x}, t_{k-1}) & \text{if } |r(\mathbf{x}, t_k)| \geq \theta_\mathcal{E}, \\ B(\mathbf{x}, t_{k-1}) & \text{otherwise.} \end{cases} \quad (16)$$

$r(\mathbf{x}, t_k)$ is reset upon a state flip to ensure each flip corresponds to a distinct contrast step and to prevent a single high-contrast edge from triggering multiple false flips. To mitigate salt-and-pepper artifacts, each flip triggers a local consistency refinement within a 3×3 window $\mathcal{W}(\mathbf{x})$ of the flipped pixel. We apply a majority vote to update $B(\mathbf{x}, t_k)$

$$B(\mathbf{x}, t_k) \leftarrow \mathbb{I}\left[\sum_{\mathbf{x}' \in \mathcal{W}(\mathbf{x})} B(\mathbf{x}', t_k) > \frac{1}{2}|\mathcal{W}(\mathbf{x})|\right], \quad (17)$$

where a pixel adopts the state shared by the majority of its neighbors. This performs asynchronously and sparsely, where only the specific small area where a change just occurred is updated rather than scanning the whole frame, thus achieving improved computational efficiency via sparse computation. In a nutshell, we keep a continuously evolving state $B(\mathbf{x}, t)$ in memory at the microsecond temporal resolution of events. Then, high-frame-rate video sequences can be generated by simply sampling this state at any desired frequency without recomputation. In this view, the video is essentially a sequence

of snapshots of this evolving state, by which we effectively decouple reconstruction frame rates from computational load.

D. Time Complexity Analysis

We analyze the computational complexity to validate the real-time capability of our method. Let N denote the spatial resolution (*i.e.*, total pixels in Ω). First, the dual-modal binarization framework incurs a cost of $\mathcal{O}(K + N)$ for event integration and pixel-wise classification over the whole spatial domain. Similarly, the log-domain variance matching estimator bypasses iterative solvers and relies on closed-form statistical moments over the sparse subset of pixels \mathbb{D} , thus limiting its complexity to a linear $\mathcal{O}(K + N)$. Both the dynamic range reshaping and the gradient-aware Otsu estimator function as lightweight statistical passes, with each contributing a bounded $\mathcal{O}(N)$ complexity. These modules are non-iterative and efficient, typically performed only upon keyframe updates.

Superior to conventional synchronous methods that scale with $\mathcal{O}(N \times \text{FPS})$ complexity², our asynchronous video generation, driven by sparse events, scales purely with the scene dynamics $\mathcal{O}(K)$. For a typical event camera (*e.g.*, DAVIS346, $N = 346 \times 260$), K represents sparse temporal changes rather than redundant dense frames. As such, our algorithm decouples computational cost from output frame rates, which allows for the generation of a kilohertz-equivalent video with constant low latency, fitting within high-speed real-time pipelines.

IV. EXPERIMENT

We use automatically calibrated c , θ_I , θ_E and empirically set $\alpha = 0.2$ and $\beta = 20$ for binarization. Five public datasets DIRD [32], HQF [49], REBlur [35], EBT [41], and RND [33] are used for qualitative or quantitative comparisons. To avoid ambiguity in ground truth (GT), evaluations are restricted to the samples exhibiting a clear bimodal distribution. Following standard practice [41], the GT for quantitative comparisons is generated from available sharp frames, where we estimate a motion-invariant threshold [13] and fine-tune it for accurate bimodal separation. Numerically, we report three widely used metrics, including the Matthews Correlation Coefficient (MCC) that measures balanced binary classification performance and remains reliable under class imbalance [50]

$$\text{MCC} = \frac{\text{TP} \cdot \text{TN} - \text{FP} \cdot \text{FN}}{\sqrt{(\text{TP} + \text{FP})(\text{TP} + \text{FN})(\text{TN} + \text{FP})(\text{TN} + \text{FN})}}, \quad (18)$$

where the above abbreviations are four confusion matrix terms, the Peak Signal-to-Noise Ratio (PSNR) that quantifies pixel-wise consistency with the GT

$$\text{PSNR} = 10 \log_{10} \left(\frac{\text{MAX}_I^2}{\text{MSE}} \right), \quad (19)$$

where $\text{MAX}_I^2 = 1$ and $\text{MSE} = (\text{FP} + \text{FN}) / (\text{TP} + \text{TN} + \text{FP} + \text{FN})$ in binarization tasks, and the Negative Rate Metric (NRM) that captures pixel-wise misclassification rates

$$\text{NRM} = \frac{1}{2} \left(\frac{\text{FN}}{\text{TP} + \text{FN}} + \frac{\text{FP}}{\text{FP} + \text{TN}} \right). \quad (20)$$

²FPS = frames per second.

The measured values are averaged over the selected samples. For those with well-balanced exposure, We further augment real-world motion blur with nighttime low light (with sensor noise) and bright glare from close-range active illumination, as challenges for robustness evaluations.

A. Binarization Results

Fig. 6 presents a visual comparison between our approach and state-of-the-art techniques, including frame-only methods (both model-based [11], [12], [15] and learning-based [17]) and a dual-modal one [41]. Our evaluation covers three challenging scenes: severe motion blur (top three rows), motion blur with low light (middle three rows), and with bright glare (bottom three rows). Frame-only ones, like human vision, degrade markedly across almost all scenarios once the frames lose informative visual cues as a result of spatial smoothing or intensity clipping. While the dual-modal competitor alleviates motion blur, it remains quite susceptible to harsh illumination. Comparatively, our method consistently recovers sharp and faithful object boundaries across all test cases even when both motion and photometric conditions are adverse, proving strong robustness to mixed degradations. Specifically, although the third-row checkerboard exhibits minor blur, most competitors fail to delineate the four corners of black squares as clearly as ours. In the fourth row, both the frame and events captured under low light are filled with noise that is disclosed by the counterparts but well suppressed in ours. These results highlight the strength of our method in maintaining reliable performance under challenging real-world environments.

Fig. 7 extends the competition by comparing ours with state-of-the-art motion deblurring methods, including frame-only [47], [48] and dual-modal ones [10], [32], [33]. The comparison features two representative scenarios: a scene with non-uniform motion blur (top) and a real-world pedestrian scene under low-light conditions with partial glare (bottom). For fair, all deblurred results are binarized using the same established baseline [11]. As illustrated, frame-only competitors struggle to produce informative reconstructions in the absence of motion and HDR cues that reveal which pixels are changing and which are hidden behind. While dual-modal deblurring methods improve sharpness via complementary event features, their resulting intensity frames still exhibit residual artifacts that can propagate and compromise the quality of subsequent binarization. This reveals the accuracy limitation of step-wise pipelines where errors accumulate across stages. In contrast, our unified single-step framework directly estimates a binary representation, bypassing intermediate reconstruction effort and error propagation. It thus consistently delivers more faithful binarization and shows reliability in real-world scenarios with complex motion patterns and mixed degradations.

Table I further reports quantitative comparisons across three datasets under varying illumination. Consistent with the visual observations, dual-modal methods outperform frame-only ones by a clear margin. Under moderate lighting, our method almost establishes the state-of-the-art and remains highly competitive with the strong baseline [41]. More importantly, it delivers impressive results under harsh imaging conditions. In challenging

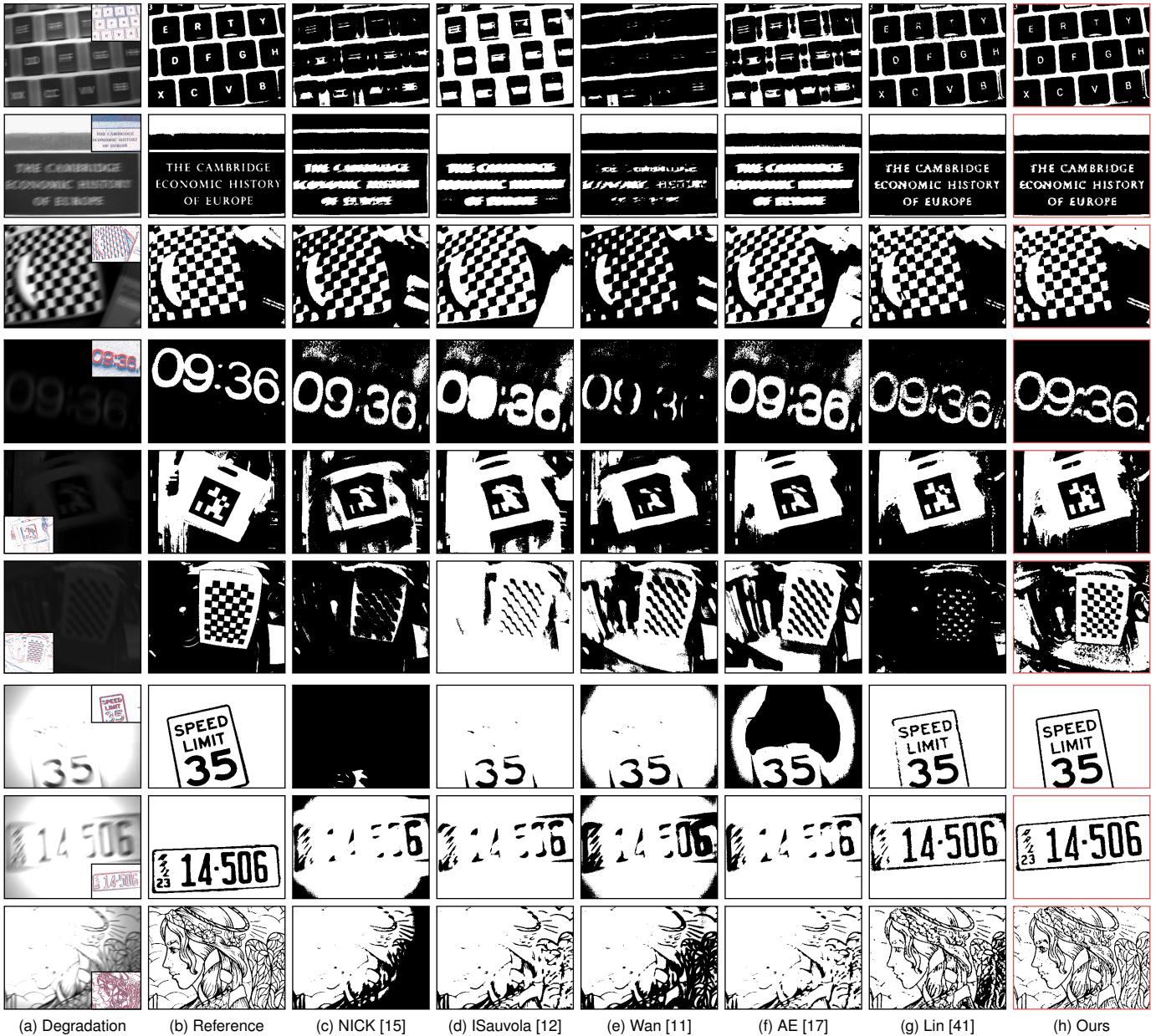


Fig. 6. Binarization results on the RND, REBlur, and EBT datasets. Each binary reference is taken from a sharp frame captured near the time of the degraded observation. The corresponding events are attached in (a) for reference.

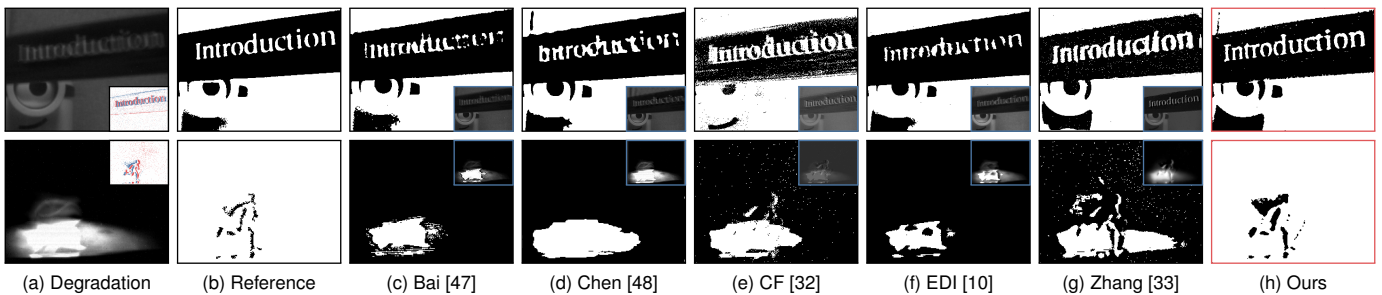


Fig. 7. Binarization results on the RND and DIRD datasets. Each binary reference is taken from a sharp frame captured near the time of the degraded observation. The corresponding events as well as the motion deblurring results are attached for reference.

low light and bright glare scenarios where the performance of the competitors severely drops, it consistently leads the runner-

TABLE I
QUANTITATIVE BINARIZATION RESULTS (WITH THE BEST AND RUNNER-UP), REPORTED AS ① MCC ↑ ② PSNR ↑ ③ NRM ↓.

Method	Dual	Gentle Light	Low Light	Bright Glare
	Modal	① / ② / ③	① / ② / ③	① / ② / ③
HQF				
NICK [15]		0.31 / 4.15 / 0.40	0.09 / 1.73 / 0.45	0.13 / 2.43 / 0.40
ISauvola [12]		0.34 / 5.03 / 0.36	0.12 / 1.75 / 0.43	0.17 / 2.89 / 0.41
Wan [11]		0.35 / 5.37 / 0.33	0.14 / 2.10 / 0.39	0.14 / 2.67 / 0.38
AE [17]		0.35 / 5.35 / 0.34	0.15 / 2.26 / 0.38	0.13 / 2.54 / 0.40
Lin [41]	✓	0.62 / 6.91 / 0.16	0.31 / 4.36 / 0.36	0.49 / 6.08 / 0.29
Bai [47]		0.23 / 3.88 / 0.43	0.08 / 1.61 / 0.47	0.10 / 1.94 / 0.40
Chen [48]		0.20 / 3.85 / 0.44	0.10 / 1.69 / 0.47	0.11 / 2.01 / 0.41
CF [32]	✓	0.48 / 5.54 / 0.30	0.23 / 3.15 / 0.33	0.32 / 5.04 / 0.31
EDI [10]	✓	0.37 / 5.13 / 0.33	0.20 / 2.34 / 0.39	0.33 / 4.96 / 0.31
Zhang [33]	✓	0.52 / 6.02 / 0.24	0.23 / 3.66 / 0.36	0.35 / 5.10 / 0.33
Ours	✓	0.62 / 6.93 / 0.21	0.48 / 6.21 / 0.26	0.54 / 6.60 / 0.25
REBlur				
NICK [15]		0.34 / 6.13 / 0.35	0.10 / 3.31 / 0.40	0.16 / 4.55 / 0.35
ISauvola [12]		0.42 / 6.25 / 0.31	0.08 / 2.94 / 0.42	0.20 / 4.97 / 0.34
Wan [11]		0.49 / 7.56 / 0.27	0.17 / 3.25 / 0.39	0.19 / 4.56 / 0.34
AE [17]		0.37 / 6.30 / 0.32	0.22 / 3.46 / 0.40	0.12 / 4.01 / 0.41
Lin [41]	✓	0.83 / 13.01 / 0.10	0.42 / 6.55 / 0.30	0.50 / 7.59 / 0.28
Bai [47]		0.40 / 6.21 / 0.30	0.22 / 3.59 / 0.44	0.14 / 4.22 / 0.41
Chen [48]		0.43 / 6.32 / 0.28	0.23 / 3.73 / 0.38	0.18 / 4.90 / 0.36
CF [32]	✓	0.59 / 8.08 / 0.19	0.34 / 5.94 / 0.33	0.40 / 6.86 / 0.31
EDI [10]	✓	0.67 / 8.77 / 0.14	0.35 / 6.12 / 0.32	0.43 / 7.29 / 0.28
Zhang [33]	✓	0.71 / 10.96 / 0.12	0.30 / 5.79 / 0.36	0.39 / 6.22 / 0.35
Ours	✓	0.86 / 13.82 / 0.08	0.65 / 8.91 / 0.20	0.59 / 8.13 / 0.24
EBT				
NICK [15]		0.28 / 6.24 / 0.40	0.07 / 2.88 / 0.47	0.10 / 2.96 / 0.45
ISauvola [12]		0.25 / 6.18 / 0.39	0.12 / 3.12 / 0.45	0.11 / 3.11 / 0.42
Wan [11]		0.31 / 7.12 / 0.37	0.15 / 3.79 / 0.44	0.17 / 4.12 / 0.37
AE [17]		0.22 / 6.04 / 0.42	0.19 / 4.01 / 0.39	0.15 / 3.97 / 0.37
Lin [41]	✓	0.79 / 14.01 / 0.20	0.43 / 7.01 / 0.32	0.59 / 10.11 / 0.27
Bai [47]		0.30 / 7.19 / 0.37	0.18 / 3.95 / 0.39	0.20 / 4.15 / 0.39
Chen [48]		0.28 / 6.13 / 0.39	0.14 / 3.70 / 0.44	0.19 / 4.23 / 0.35
CF [32]	✓	0.54 / 9.53 / 0.33	0.27 / 5.96 / 0.35	0.30 / 6.32 / 0.38
EDI [10]	✓	0.59 / 10.01 / 0.28	0.29 / 6.15 / 0.36	0.35 / 7.10 / 0.35
Zhang [33]	✓	0.65 / 11.79 / 0.24	0.32 / 6.93 / 0.33	0.41 / 7.25 / 0.34
Ours	✓	0.73 / 13.67 / 0.18	0.54 / 7.32 / 0.29	0.66 / 10.53 / 0.22

up across all evaluation metrics by a wide margin.

B. Downstream Tasks

High-quality binarization provides a compact yet informative source that benefits a range of downstream tasks in both accuracy and computational efficiency. Fig. 8 illustrates the superiority of our approach across three representative applications, including OCR, fiducial marker tracking, and optical flow estimation, under diverse lighting. These tasks often place strict demands on input quality, in which minor distortions or information loss can clearly compromise performance. We exploit the popular learning-based techniques EasyOCR [51], [52], DeepTag [53], and RAFT [54] for downstream analysis. As seen from the comparison, the degraded frames and competing methods produce low-quality, ambiguous inputs that often mislead downstream algorithms, leading to recognition faults in OCR, imprecise corner localization in marker tracking, and unfaithful, inconsistent boundary preservation in optical flow estimation. Comparatively, our method generates clean and structurally faithful binary representations that preserve critical scene geometry. This enables reliable text recognition, stable keypoint localization for fiducials, and coherent boundary-aware motion estimation.

Table II further reports quantitative evaluations for these downstream tasks, averaged over six frames captured at dif-

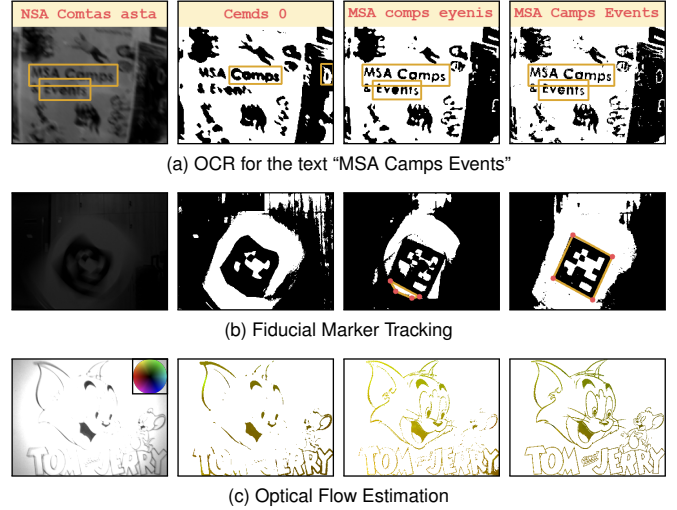


Fig. 8. Accurate binarization benefits a range of downstream tasks. Left to right: degraded frames, ISauvola [12], Lin [41], and Ours. The samples are taken from the HQF and EBT datasets.

TABLE II
BINARIZATION FOR DOWNSTREAM TASKS UNDER VARYING LIGHTING CONDITIONS (① GENTLE LIGHT ② LOW LIGHT ③ BRIGHT GLARE), REPORTED AS CER ↓, RMSE ↓, AND AEPE ↓ RESPECTIVELY.

Method	Dual	OCR	Tracking	Optical Flow
	Modal	① / ② / ③	① / ② / ③	① / ② / ③
ISauvola [12]		0.62 / 0.82 / 0.79	4.25 / 7.72 / 8.91	7.62 / 11.85 / 12.01
Bai [47]		0.54 / 0.73 / 0.71	3.41 / 6.84 / 7.68	6.24 / 9.76 / 9.44
Zhang [33]	✓	0.38 / 0.48 / 0.49	1.72 / 4.92 / 5.62	4.15 / 7.82 / 7.56
Lin [41]	✓	0.21 / 0.37 / 0.35	1.36 / 3.78 / 4.01	2.53 / 6.15 / 6.01
Ours	✓	0.19 / 0.29 / 0.23	1.36 / 2.41 / 2.86	2.41 / 4.92 / 4.53

ferent timestamps. For each task, we use the Character Error Rate (CER) to assess the fraction of incorrect letters, the Root Mean Square Error (RMSE) to quantify pixel-wise localization errors of detected marker corners, and the Average Endpoint Error (AEPE) to measure the deviation of the predicted optical flow fields from the GT. In line with the visual observations, frame-only methods struggle across all tasks even under gentle lighting due to unresolved motion blur, whereas dual-modal counterparts improve by a clear margin. Specifically, our approach yields sharp, reliable binary representations that keep lower error rates across all three applications. These findings suggest that our solution has stronger potential to serve as a robust and efficient foundation for a wide range of downstream visual tasks, especially under challenging imaging conditions.

C. High-Frame-Rate Video Analysis

Fig. 9 shows a stress test on how frame rates influence binarization quality and downstream OCR performance, where our visual results at three distinct timestamps are given along with the comparisons against representative EDI [10] on the MCC and CER metrics, evaluated over six frames at different time. The curves reveal a clear advantage of our asynchronous event-driven residual update over the synchronous time-binning. As frame rates grow, EDI degrades significantly since a narrowing time window reduces event counts available for computation, leaving ineffective temporal integration and poor reconstruct-

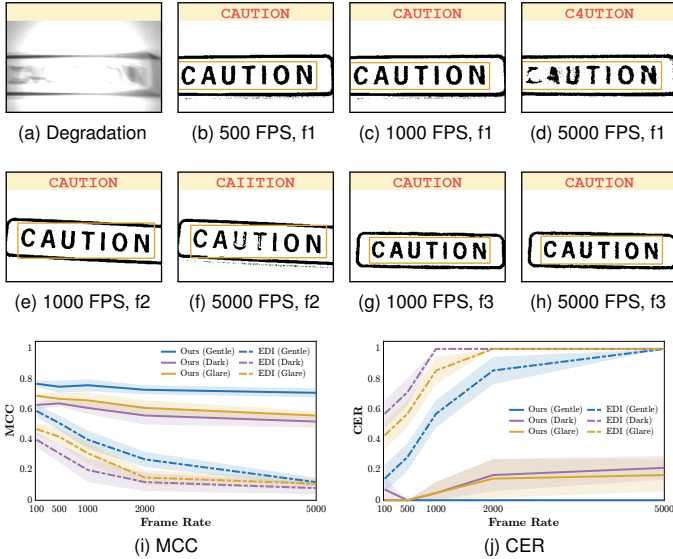


Fig. 9. High-frame-rate binary videos. (b)–(h) present our results for 3 frames at different time under bright glare, and (i)–(j) provide the comparisons under three lighting conditions. The sample is taken from the EBT dataset.

tion. In comparison, our asynchronous operation maintains a continuously evolving state to bypass the information scarcity of fixed temporal slices, enabling consistent binary results even at kilohertz frame rates. This proves that our scalable approach better aligns with the asynchronous nature of event cameras. Moreover, a slight dip is observed at 5000 FPS. Rather than an algorithmic flaw, it reflects sensor-level constraints, including timestamp jitter and readout bandwidth under high event rates, as well as the effect of capturing asynchronous update mid-transition. Overall, these results confirm that our method scales gracefully with extreme frame rates while preserving stable binarization and downstream task reliability.

A clear distinction should be made between event scarcity at a scene level and within a fixed time slot. Naturally, dual-modal methods struggle when a scene triggers very few events (*e.g.*, a near-static scene), since they basically revert to frame-only baselines. Conversely, the study in Fig. 9 examines the contribution of events per time slot in scenarios already filled with abundant event activity, where we focus on the ability of efficient information aggregation under limited temporal resolution. While our method can theoretically scale to 10000 FPS (bounded by the time resolution of event cameras), we report our findings at 5000 FPS, which already satisfies most real-world dynamic applications.

D. Runtime Analysis

Fig. 10 presents a runtime evaluation across four datasets, each comprising six sequences with varying temporal lengths and event counts (*i.e.*, event rates spanning both sparse and dense scenes). All evaluated methods run on an Apple M4 Pro chip using a single CPU core without GPU acceleration, to ensure a fair and hardware-consistent comparison. We report four metrics, including the total runtime, real-time factor (sequence length/runtime), processing rate (event counts/runtime), and

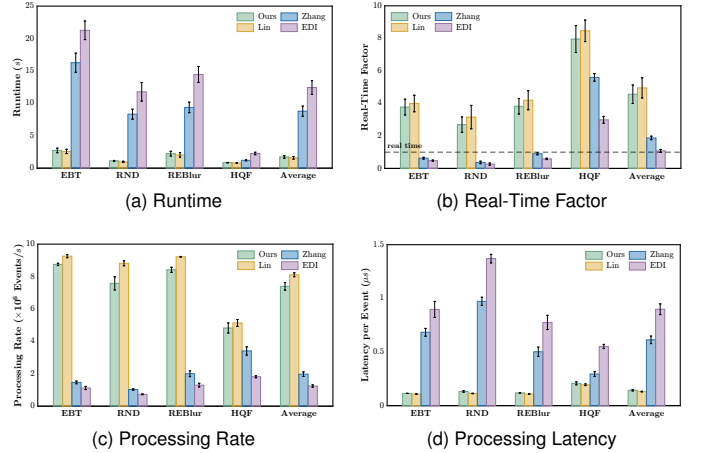


Fig. 10. Runtime performance across the datasets with varying event rates.

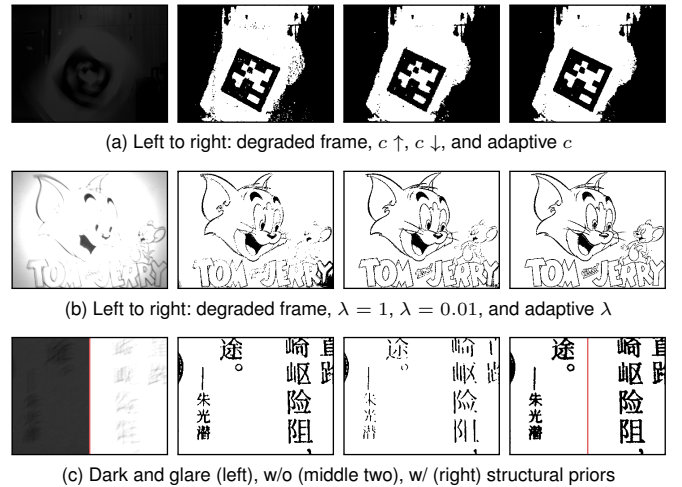


Fig. 11. Adaptive parameters optimize binarization results.

processing latency (runtime/event counts). Notably, a real-time factor higher than 1 indicates that a method processes an event stream faster than its physical acquisition time and thus operates in real time. As illustrated, our approach minimizes runtime to perform on par with the fastest baseline [41] and consistently keeps real-time performance across all tested sequences with either sparse or dense event streams, whereas the two step-wise pipelines take more runtime overhead. Besides, our method sustains a high event processing throughput, making it possible to operate in step with ultra-fast, low-latency event cameras. While not yet tested on actual resource-constrained mobile systems, the relative efficiency gains observed in this controlled environment indicate our stronger potential for deployment on edge devices in high-speed, real-time robotic applications.

E. Ablation Study

We conduct an ablation study on the EBT dataset to analyze the contribution of the key components in our dual-modal binarization framework. Specifically, we investigate: (i) manually setting the contrast threshold c to values lower (\downarrow) or higher (\uparrow) than the adaptively estimated one, (ii) varying the strength

TABLE III
EVALUATIONS OF PARAMETER SETTINGS ON THE EBT DATASET (WITH THE BEST), REPORTED AS ① MCC ↑ ② PSNR ↑ ③ NRM ↓.

Parameter	Value	Gentle Light	Low Light	Bright Glare
		① / ② / ③	① / ② / ③	① / ② / ③
c	↑	0.71 / 13.33 / 0.22	0.48 / 6.84 / 0.31	0.62 / 10.09 / 0.24
	↓	0.70 / 13.42 / 0.22	0.45 / 7.01 / 0.33	0.65 / 10.39 / 0.23
	Adaptive	0.73 / 13.67 / 0.18	0.54 / 7.32 / 0.29	0.66 / 10.53 / 0.22
λ	1	0.65 / 13.02 / 0.21	0.45 / 6.80 / 0.32	0.60 / 10.35 / 0.26
	0.01	0.68 / 12.87 / 0.20	0.51 / 6.89 / 0.32	0.64 / 10.06 / 0.23
	Adaptive	0.73 / 13.67 / 0.18	0.54 / 7.32 / 0.29	0.66 / 10.53 / 0.22
$g(\theta)$	$e - 1^\dagger$	0.71 / 13.33 / 0.20	0.51 / 7.14 / 0.30	0.60 / 10.19 / 0.27
	Adaptive	0.73 / 13.67 / 0.18	0.54 / 7.32 / 0.29	0.66 / 10.53 / 0.22

† Eq. (12) is spatially blind to structural cues when $g(\theta) = e - 1$.

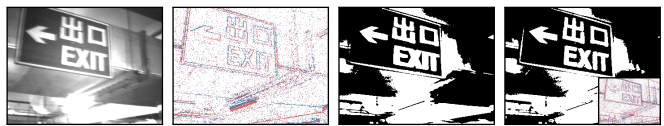
of dynamic range reshaping, and (iii) disabling gradient priors during threshold estimation. As shown in Fig. 11, setting c to a higher value amplifies noise, while a lower value weakens structure reshaping. Similarly, suboptimal fusion strength between degraded frames and events introduces distinct artifacts. Insufficient event contribution results in structural loss due to highlight clipping, whereas excessive reliance on sparse events causes spatial jitter and fragmented, discontinuous contours. These findings highlight the value of adaptive parameter estimation over fixed settings across diverse scenarios. Besides, incorporating the proposed statistical–structural coupling during threshold estimation ensures more faithful binarization, particularly under challenging photometric conditions. The quantitative results in Table III are consistent with these visual observations and provide clear evidence of the effectiveness of each component in the overall framework.

F. Event Quality for Binarization

Dual-modal fusion is influenced not only by the quality of degraded frames but also by that of event streams. However, sensitive event cameras are susceptible to environmental interference and then respond to complex scene dynamics with non-ideal events [55]. This motivates a study on how event quality impacts binarization performance. In Fig. 12 (a), we present results based on the events with real-world background activity noise induced by light flickering. Such false events in low-frequency regions account for a dominant proportion and corrupt the dual-modal fusion. As a result, the sharp intensity frame of Zhang [33] is overwhelmed by the noise that then leads to an inferior binary result, whereas our method filters out these uncorrelated perturbations and still delivers clean, recognizable letters and sharp boundaries. Fig. 12 (b) shows a case when sparse events from minimal motion are insufficient to complement structural cues, causing the degraded frame to dominate and yield suboptimal binarization (*e.g.*, the unclear “X” in “EXIT”). For comparison, we also present an improved outcome at a later timestamp where stronger motion brings a denser event stream. To further validate these visual findings, Fig. 12 (c) and (d) examine the response of our method to synthetic Poisson noise and random event dropout, evaluating six frames at different time within the same sequence under three lighting conditions. The variances indicate that while our method remains robust to moderate noise interference, it is not



(a) Left to right: blurry frame, events with real-world noise, Zhang [33], and Ours



(b) Left to right: blurry frame, sparse events, Ours, and Ours at another time

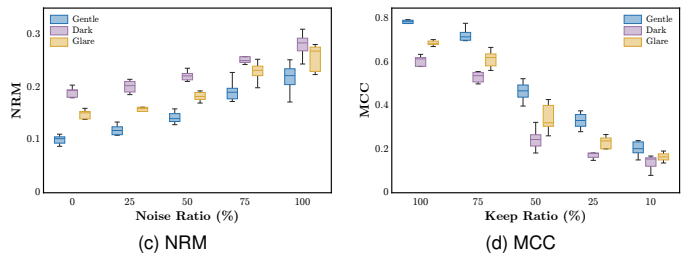


Fig. 12. Evaluation of the impact of event quality on binarization. The samples are taken from the RND and EBT datasets.

resilient to event scarcity in near-static scenes where neither modality conveys adequate discriminative features.

V. CONCLUSION

This work proposes a lightweight dual-modal approach that bridges the features of frames and events to enable real-time, high-frame-rate binarization on CPU-only systems. Extensive experiments on real-world datasets demonstrate competitive performance in mitigating motion blur and clear advantages under harsh illumination, with additional benefits for downstream tasks. Despite the strengths, our current evaluation is limited to desktop-class hardware, and the method has not yet been validated on resource-constrained mobile or embedded devices. Future work will focus on efficient deployment and optimization on edge platforms, with particular interest in embedded robotic systems. One promising direction is underwater inspection, where our approach could facilitate robust, real-time cable and infrastructure analysis under low-visibility and dynamic lighting conditions.

ACKNOWLEDGMENTS

We express our gratitude to Rongzhou Chen (PhD student, The University of Hong Kong) for his valuable discussions and assistance. We also thank the Imaging Systems Laboratory at The University of Hong Kong for supplying event cameras. This work was supported in part by the Guangxi University Talent Development Funding, the National Natural Science Foundation of China (62505167), and the Science and Technology Commission of Shanghai Municipality (25ZR1402149).

REFERENCES

- [1] S. Wang, M. Zhu, Y. Hu, D. Li, F. Yuan, and J. Yu, “CylinderTag: an accurate and flexible marker for cylinder-shape objects pose estimation based on projective invariants,” *IEEE Transactions on Visualization and Computer Graphics*, vol. 30, no. 12, pp. 7486–7499, 2024.

- [2] A. Phung, G. Billings, A. F. Daniele, M. R. Walter, and R. Camilli, "A shared autonomy system for precise and efficient remote underwater manipulation," *IEEE Transactions on Robotics*, vol. 40, pp. 4147–4159, 2024.
- [3] S. Ghosh and G. Gallego, "Event-based stereo depth estimation: a survey," *IEEE Transactions on Pattern Analysis and Machine Intelligence*, vol. 47, no. 10, pp. 9130–9149, 2025.
- [4] G. Gallego, T. Delbruck, G. M. Orchard, C. Bartolozzi, B. Taba, A. Censi, S. Leutenegger, A. Davison, J. Conradt, K. Daniilidis, and D. Scaramuzza, "Event-based vision: a survey," *IEEE Transactions on Pattern Analysis and Machine Intelligence*, vol. 44, no. 1, pp. 154–180, 2022.
- [5] D. Gehrig and D. Scaramuzza, "Low-latency automotive vision with event cameras," *Nature*, vol. 629, pp. 1034–1040, 2024.
- [6] Y. Deng, H. Chen, H. Chen, and Y. Li, "Learning from images: a distillation learning framework for event cameras," *IEEE Transactions on Image Processing*, vol. 30, pp. 4919–4931, 2021.
- [7] Y. Zhu and L. F. Tadesse, "SpectroGen: a physically informed generative artificial intelligence for accelerated cross-modality spectroscopic materials characterization," *Matter*, vol. 9, no. 1, p. 102434, 2026.
- [8] Y. Qi, L. Zhu, Y. Zhao, N. Bao, and J. Li, "Deblurring neural radiance fields with event-driven bundle adjustment," in *Proceedings of the 32nd ACM International Conference on Multimedia (ACM MM)*, 2024, pp. 9262–9270.
- [9] W. Yang, J. Wu, L. Li, W. Dong, and G. Shi, "Event-based motion deblurring with modality-aware decomposition and recomposition," in *Proceedings of the 31st ACM International Conference on Multimedia (ACM MM)*, 2023, pp. 8327–8335.
- [10] L. Pan, C. Scheerlinck, X. Yu, R. Hartley, M. Liu, and Y. Dai, "Bringing a blurry frame alive at high frame-rate with an event camera," in *Proceedings of the IEEE/CVF Conference on Computer Vision and Pattern Recognition (CVPR)*, 2019, pp. 6820–6829.
- [11] W. A. Mustafa and M. M. M. Abdul Kader, "Binarization of document image using optimum threshold modification," in *Journal of Physics: Conference Series*, vol. 1019, 2018, p. 012022.
- [12] Z. Hadjadj, A. Meziane, Y. Cherfa, M. Cheriet, and I. Setitra, "ISauvola: improved Sauvola's algorithm for document image binarization," in *International Conference on Image Analysis and Recognition*, 2016, pp. 737–745.
- [13] N. Otsu, "A threshold selection method from gray-level histograms," *IEEE Transactions on Systems, Man, and Cybernetics*, vol. 9, no. 1, pp. 62–66, 1979.
- [14] B. Su, S. Lu, and C. L. Tan, "Robust document image binarization technique for degraded document images," *IEEE Transactions on Image Processing*, vol. 22, no. 4, pp. 1408–1417, 2013.
- [15] K. Khurshid, I. Siddiqi, C. Faure, and N. Vincent, "Comparison of Niblack inspired binarization methods for ancient documents," in *Document Recognition and Retrieval XVI*, vol. 7247, 2009, pp. 267–275.
- [16] S. He and L. Schomaker, "DeepOtsu: document enhancement and binarization using iterative deep learning," *Pattern Recognition*, vol. 91, pp. 379–390, 2019.
- [17] J. Calvo-Zaragoza and A.-J. Gallego, "A selectional auto-encoder approach for document image binarization," *Pattern Recognition*, vol. 86, pp. 37–47, 2019.
- [18] C. Qu, Z. Chen, J. Zhang, X. Chen, and J. Han, "Self-BSR: self-supervised image denoising and destriping based on blind-spot regularization," *IEEE Transactions on Circuits and Systems for Video Technology*, vol. 35, no. 9, pp. 8666–8678, 2025.
- [19] A. Sulaiman, K. Omar, and M. F. Nasrudin, "Degraded historical document binarization: a review on issues, challenges, techniques, and future directions," *Journal of Imaging*, vol. 5, no. 4, p. 48, 2019.
- [20] P. Duan, B. Li, Y. Yang, H. Lou, M. Teng, X. Zhou, Y. Ma, and B. Shi, "EventAid: benchmarking event-aided image/video enhancement algorithms with real-captured hybrid dataset," *IEEE Transactions on Pattern Analysis and Machine Intelligence*, vol. 47, no. 8, pp. 6959–6973, 2025.
- [21] D. Falanga, K. Kleber, and D. Scaramuzza, "Dynamic obstacle avoidance for quadrotors with event cameras," *Science Robotics*, vol. 5, no. 40, p. eaaz9712, 2020.
- [22] G. Magrini, L. Berlincioni, F. Becattini, L. Cultrera, and P. Pala, "Drone detection with event cameras," in *Proceedings of the IEEE/CVF International Conference on Computer Vision Workshops (ICCVW)*, 2025, pp. 4703–4714.
- [23] S. Zhu, Q. Yin, C. Wang, J. Huang, and E. Y. Lam, "Ultrafast dynamic defect inspection with computational neuromorphic imaging," *Advanced Science*, vol. 12, no. 44, p. e10338, 2025.
- [24] Z. Ge, H. Wei, F. Xu, Y. Gao, Z. Chu, H. K.-H. So, and E. Y. Lam, "Millisecond autofocusing microscopy using neuromorphic event sensing," *Optics and Lasers in Engineering*, vol. 160, p. 107247, 2023.
- [25] C. Wang, S. Zhu, P. Zhang, K. Wang, J. Huang, and E. Y. Lam, "Angle-based neuromorphic wave normal sensing," *Laser & Photonics Reviews*, vol. 19, no. 4, p. 2400647, 2025.
- [26] Z. Du, M. Gupta, F. Xu, K. Zhang, J. Zhang, Y. Zhou, Y. Liu, Z. Wang, J. Wrachtrup, N. Wong, C. Li, and Z. Chu, "Widefield diamond quantum sensing with neuromorphic vision sensors," *Advanced Science*, vol. 11, no. 2, p. 2304355, 2024.
- [27] R. Guo, Q. Yang, A. S. Chang, G. Hu, J. Greene, C. V. Gabel, S. You, and L. Tian, "EventLFM: event camera integrated Fourier light field microscopy for ultrafast 3D imaging," *Light: Science & Applications*, vol. 13, p. 144, 2024.
- [28] P. Zhang, S. Zhu, C. Wang, Y. Zhao, and E. Y. Lam, "Neuromorphic imaging with super-resolution," *IEEE Transactions on Circuits and Systems for Video Technology*, vol. 35, no. 2, pp. 1715–1727, 2025.
- [29] R. Chen, C. Wang, Y. Li, Y. Cao, S. Zhu, and E. Y. Lam, "Self-calibrated neuromorphic hyperspectral derivative imaging," *Optica*, vol. 13, no. 4, pp. 587–590, 2026.
- [30] S. Lin, G. Zheng, Z. Wang, R. Han, W. Xing, Z. Zhang, Y. Peng, and J. Pan, "Embodied neuromorphic synergy for lighting-robust machine vision to see in extreme bright," *Nature Communications*, vol. 15, p. 10781, 2024.
- [31] H. Wang, R. Guo, P. Ma, C. Ruan, X. Luo, W. Ding, T. Zhong, J. Xu, Y. Liu, and X. Chen, "Event camera meets mobile embodied perception: abstraction, algorithm, acceleration, application," *ACM Computing Surveys*, vol. 58, no. 8, pp. 1–41, 2026.
- [32] C. Scheerlinck, N. Barnes, and R. Mahony, "Continuous-time intensity estimation using event cameras," in *Asian Conference on Computer Vision (ACCV)*, 2018, pp. 308–324.
- [33] P. Zhang, H. Liu, Z. Ge, C. Wang, and E. Y. Lam, "Neuromorphic imaging with joint image deblurring and event denoising," *IEEE Transactions on Image Processing*, vol. 33, pp. 2318–2333, 2024.
- [34] H. Rebecq, R. Ranftl, V. Koltun, and D. Scaramuzza, "High speed and high dynamic range video with an event camera," *IEEE Transactions on Pattern Analysis and Machine Intelligence*, vol. 43, no. 6, pp. 1964–1980, 2021.
- [35] L. Sun, C. Sakaridis, J. Liang, Q. Jiang, K. Yang, P. Sun, Y. Ye, K. Wang, and L. V. Gool, "Event-based fusion for motion deblurring with cross-modal attention," in *European Conference on Computer Vision (ECCV)*, 2022, pp. 412–428.
- [36] J. Wu, P. Duan, Z. Wang, C. Wang, B. Shi, and E. Y. Lam, "Dark-EvGS: event camera as an eye for radiance field in the dark," *IEEE Transactions on Image Processing*, vol. 35, pp. 3172–3185, 2026.
- [37] S. Xu, Z. Sun, M. Zhong, C. Cao, Y. Liu, X. Fu, and Y. Chen, "Motion-adaptive Transformer for event-based image deblurring," in *Proceedings of the AAAI Conference on Artificial Intelligence (AAAI)*, vol. 39, no. 9, 2025, pp. 8942–8950.
- [38] Z. Xiao and X. Wang, "Event-based video super-resolution via state space models," in *Proceedings of the IEEE/CVF Conference on Computer Vision and Pattern Recognition (CVPR)*, 2025, pp. 12 564–12 574.
- [39] X. Xie, Q. Zhang, and W.-S. Zheng, "Diffusion-based event generation for high-quality image deblurring," in *Proceedings of the IEEE/CVF Conference on Computer Vision and Pattern Recognition (CVPR)*, 2025, pp. 2194–2203.
- [40] Y. Yang, J. Zhang, Y. Zhang, Y. Wei, D. Zou, J. S. Ren, and B. Shi, "Event-guided HDR reconstruction with diffusion priors," in *Proceedings of the IEEE/CVF International Conference on Computer Vision (ICCV)*, 2025, pp. 11 787–11 796.
- [41] S. Lin, X. Zhang, L. Yang, L. Yu, B. Zhou, X. Luo, W. Wang, and J. Pan, "Neuromorphic synergy for video binarization," *IEEE Transactions on Image Processing*, vol. 33, pp. 1403–1418, 2024.
- [42] C. Brander, G. Cioffi, N. Messikommer, and D. Scaramuzza, "Reading in the dark with foveated event vision," in *Proceedings of the IEEE/CVF Conference on Computer Vision and Pattern Recognition Workshops (CVPRW)*, 2025, pp. 5044–5052.
- [43] G. Taverni, D. P. Moeys, C. Li, C. Cavaco, V. Motsnyi, D. S. S. Bello, and T. Delbruck, "Front and back illuminated dynamic and active pixel vision sensors comparison," *IEEE Transactions on Circuits and Systems II: Express Briefs*, vol. 65, no. 5, pp. 677–681, 2018.
- [44] G. Gallego, H. Rebecq, and D. Scaramuzza, "A unifying contrast maximization framework for event cameras, with applications to motion, depth, and optical flow estimation," in *Proceedings of the IEEE/CVF Conference on Computer Vision and Pattern Recognition (CVPR)*, 2018, pp. 3867–3876.

- [45] P. Zhang, S. Zhu, and E. Y. Lam, "Event encryption: rethinking privacy exposure for neuromorphic imaging," *Neuromorphic Computing and Engineering*, vol. 4, no. 1, p. 014002, 2024.
- [46] Z. Wang, Y. Ng, P. van Goor, and R. Mahony, "Event camera calibration of per-pixel biased contrast threshold," in *Australasian Conference of Robotics and Automation (ACRA)*, 2019.
- [47] Y. Bai, G. Cheung, X. Liu, and W. Gao, "Graph-based blind image deblurring from a single photograph," *IEEE Transactions on Image Processing*, vol. 28, no. 3, pp. 1404–1418, 2019.
- [48] L. Chen, F. Fang, T. Wang, and G. Zhang, "Blind image deblurring with local maximum gradient prior," in *Proceedings of the IEEE/CVF Conference on Computer Vision and Pattern Recognition (CVPR)*, 2019, pp. 1742–1750.
- [49] T. Stoffregen, C. Scheerlinck, D. Scaramuzza, T. Drummond, N. Barnes, L. Kleeman, and R. Mahony, "Reducing the sim-to-real gap for event cameras," in *European Conference on Computer Vision (ECCV)*, 2020, pp. 534–549.
- [50] D. Chicco and G. Jurman, "The advantages of the Matthews correlation coefficient (MCC) over F1 score and accuracy in binary classification evaluation," *BMC Genomics*, vol. 21, p. 6, 2020.
- [51] Y. Baek, B. Lee, D. Han, S. Yun, and H. Lee, "Character region awareness for text detection," in *Proceedings of the IEEE/CVF Conference on Computer Vision and Pattern Recognition (CVPR)*, 2019, pp. 9365–9374.
- [52] B. Shi, X. Bai, and C. Yao, "An end-to-end trainable neural network for image-based sequence recognition and its application to scene text recognition," *IEEE Transactions on Pattern Analysis and Machine Intelligence*, vol. 39, no. 11, pp. 2298–2304, 2017.
- [53] Z. Zhang, Y. Hu, G. Yu, and J. Dai, "DeepTag: a general framework for fiducial marker design and detection," *IEEE Transactions on Pattern Analysis and Machine Intelligence*, vol. 45, no. 3, pp. 2931–2944, 2023.
- [54] Z. Teed and J. Deng, "RAFT: recurrent all-pairs field transforms for optical flow," in *European Conference on Computer Vision (ECCV)*, 2020, pp. 402–419.
- [55] P. Zhang, Z. Ge, L. Song, and E. Y. Lam, "Neuromorphic imaging with density-based spatiotemporal denoising," *IEEE Transactions on Computational Imaging*, vol. 9, pp. 530–541, 2023.